J. Fluid Mech. (2026), *vol.* 1040, A12, doi:10.1017/jfm.2026.11852



Optimal airfoils in the intermediate-Reynolds-number range

Gleb Zhdanko[1] and **Dmitry Kolomenskiy**[1]

[1]Center for Materials Technologies, Skolkovo Institute of Science and Technology, Moscow, Russia

Corresponding author: Dmitry Kolomenskiy, dkolom@gmail.com

(Received 13 May 2026 UTC; revised 20 June 2026 UTC; accepted 26 June 2026 UTC)

We revisit a classical airfoil design problem: the search for shapes that maximise aerodynamic performance metrics, targeting the underexplored intermediate Reynolds-number regime between 1 and 3000, relevant to small animals and miniature vehicles. The problem is formally stated as the glide ratio or the endurance factor maximisation for Joukowski airfoil profiles and for more general airfoil shapes with adjustable position of the maximum camber, under steady inflow. It is solved numerically by a hybrid approach combining stochastic search and direct parameter sweep, and using a steady laminar Navier–Stokes solver based on conformal mapping and second-order finite-difference discretisation. Zero-thickness cambered airfoils are found to be globally optimal, within the Joukowski family, across the entire Reynolds-number range considered. The optimal angle of attack decreases monotonically with the Reynolds number (Re), whereas the optimal camber varies non-monotonically, reaching a pronounced maximum near $Re \approx 40-50$ before declining at higher Re. At low Reynolds numbers ($Re \lesssim 100$), a broad family of cambered shapes performs within a few per cent of the optimum, indicating weak sensitivity to geometrical parameters. In contrast, for $Re \gtrsim 1000$, the performance landscape becomes sharply localised around a single preferred design, for which geometric refinement is critical.

Key words: aerodynamics, swimming/flying

1. Introduction

Lift and propulsion mechanisms in fluids have been extensively studied across a wide range of the Reynolds numbers (Re). At high Re ($> 10^4$), typical of aeronautical applications, the literature is rich with theoretical, computational and experimental insights. Decades of research have established that cambered thin-plate airfoils ensure optimal lift-to-drag ratios for the range of Re up to 10^5. Low-Re regimes ($Re \ll 1$), typical of microbial swimmers, have also received substantial attention. Here, the Stokes flow

© The Author(s), 2026. Published by Cambridge University Press.

https://doi.org/10.1017/jfm.2026.11852 Published online by Cambridge University Press

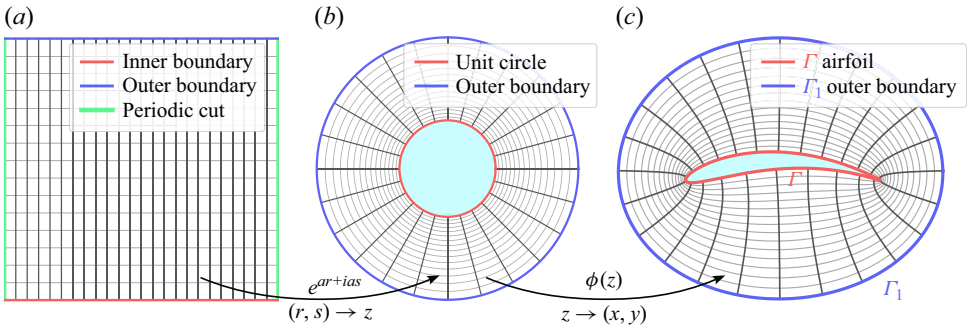


Figure 1. The three-stage conformal mapping: (*a*) rectangular computational domain in (r, s) coordinates; (*b*) intermediate annular domain in the z-plane; (*c*) physical domain with the body-fitted grid to the airfoil surface. Inner and outer boundaries are shown in red and blue, respectively.

approximation enables analytical solutions yielding explicit formulas for the fluid-dynamic forces. Intermediate Re values ($1 \lesssim Re \lesssim 10\,000$), prevalent in biological locomotion, have historically received less attention. This gap likely stems from analytical intractability (viscous and inertial effects compete without simplifying assumptions) and experimental challenges: neither traditional high-Re wind tunnels nor microfluidic set-ups can reliably cover this range of Re. Recent technological advances in bio-inspired micro air vehicles have spurred practical interest in this flow regime.

Studies on insect flight ($Re \sim 10$–1000) often employ flat, cambered or even corrugated thin foils as wing models. Yet, systematic efforts to identify optimal airfoil shapes remain scarce, with most work prioritising kinematics over geometry. A notable exception is the shape-optimisation study by Srinath & Mittal (2009), which explored a broad parameter space of airfoil contours at fixed angles of attack ($\alpha = 4°$ and $12°$) using adjoint optimisation. However, the complex shapes obtained therein reflect the α constraint rather than the necessity of non-zero thickness. Our present study addresses this problem through a low-dimensional parameterisation of airfoil profiles, enabling efficient exploration of the combined effect of main features of the shape (i.e. thickness and camber) and angle of attack across intermediate Re. By coupling a parametric geometrical description with Navier–Stokes simulations, we identify optimal airfoils within the Joukowski family, then more general airfoil shapes with adjustable position of the maximum camber. We relate the observed trends of the optimal parameters as functions of Re to the competing effect of camber-enhanced lift and inertia-driven separation.

2. Mathematical model

2.1. *Governing equations*

Airfoil optimisation requires flow solutions for many candidate profiles, making repeated mesh generation computationally expensive. We avoid this by using conformal mapping, which simultaneously defines the airfoil, generates an orthogonal grid and yields the metric terms for the transformed Navier–Stokes equations. The map is constructed in two stages, mapping the airfoil exterior to the computational domain via an intermediate annular domain (see figure 1). The starting point is a rectangular grid in (r, s) coordinates, where r is the radial coordinate and s the periodic angular coordinate. The first map, $z = e^{ar+\mathrm{i}as}$, where the parameter $a \in \mathbb{R}$ controls the grid stretching, deforms this rectangular grid into an O-grid in the complex z-plane: lines of constant r become

https://doi.org/10.1017/jfm.2026.11852 Published online by Cambridge University Press

concentric circles, and lines of constant s become radial rays. The second map, ϕ, from the annulus onto the airfoil exterior, $x + \mathrm{i}y = \phi(z)$, deforms the O-grid into a body-fitted mesh, with the inner boundary conforming to the airfoil surface Γ and the outer boundary mapped to the far-field boundary Γ_1. We will examine two sets of results using two different maps $\phi(z)$: Joukowski transform (§ 2.3) and Wegmann transform (§ 2.4). With the composite mapping defined, the incompressible steady Navier–Stokes equations in vorticity–streamfunction form can be rewritten in (r, s) coordinates. Denoting $A = \mathrm{Re}(\phi'(z)az)$ and $B = \mathrm{Im}(\phi'(z)az)$, the Jacobian of the transformation $(r, s) \to (x, y)$ is $\boldsymbol{J} = \left(\begin{smallmatrix} A & -B \\ B & A \end{smallmatrix}\right)$, and the governing equations are written in computational coordinates

$$\frac{1}{\det \boldsymbol{J}}\left(\frac{\partial \psi}{\partial s}\frac{\partial \omega}{\partial r} - \frac{\partial \psi}{\partial r}\frac{\partial \omega}{\partial s}\right) = \frac{1}{Re}\frac{1}{\det \boldsymbol{J}}\nabla^2_{r,s}\omega, \tag{2.1}$$

$$\omega = -\frac{1}{\det \boldsymbol{J}}\nabla^2_{r,s}\psi, \tag{2.2}$$

where ω is the vorticity, ψ is the streamfunction, $Re = \rho U_\infty c/\mu$, ρ is the fluid density, U_∞ the free-stream velocity, c the chord length and μ the dynamic viscosity.

2.2. *Boundary conditions*

On the airfoil surface Γ, the no-penetration and no-slip conditions are $\partial\psi/\partial \boldsymbol{n} = 0$ and $\partial\psi/\partial \boldsymbol{\tau} = 0$, where $\boldsymbol{n}$ and $\boldsymbol{\tau}$ denote the unit normal and unit tangent vector to Γ, respectively. Since conformal maps preserve orthogonality, the conditions retain their form in (r, s) coordinates. From the boundary condition $\partial\psi/\partial s = 0$ on Γ, it follows that ψ is uniform on the airfoil surface. Since ψ is defined only up to an additive constant, this value may be chosen as zero, reducing the boundary conditions to $\psi = 0$ and $\partial\psi/\partial r = 0$ on Γ.

At the outer boundary Γ_1, uniform horizontal free-stream conditions are imposed, which in terms of the streamfunction read $\partial\psi/\partial y = 1$, $\partial\psi/\partial x = 0$ on Γ_1. Applying the chain rule for the conformal transformation yields the outer boundary conditions

$$\psi_r = B, \quad \psi_s = A \quad \text{on} \quad \Gamma_1. \tag{2.3a,b}$$

At the continuous level, both conditions (2.3) are valid and equivalent representations of the imposed far-field velocity. However, in the discrete formulation, prescribing both streamfunction derivatives simultaneously leads to an ill-conditioned system when coupled with the Poisson equation (2.2). Condition (2.3*a*) is retained as it directly controls the mass flux through the outer boundary, whereas condition (2.3*b*) is redundant given the irrotationality of the undisturbed free stream and therefore dropped in favour of the vorticity condition $\omega = 0$. This substitution restores well-posedness of the discrete system without altering the physical model, yielding the system

$$\left(\frac{\partial \psi}{\partial s}\frac{\partial \omega}{\partial r} - \frac{\partial \psi}{\partial r}\frac{\partial \omega}{\partial s}\right) = \frac{1}{Re}\nabla^2_{r,s}\omega, \qquad \omega = -\frac{1}{\det \boldsymbol{J}}\nabla^2_{r,s}\psi, \qquad \text{with B.C.} \quad \begin{array}{llll} \psi = 0, & \dfrac{\partial \psi}{\partial r} = 0 & \text{on } \Gamma, \\ \dfrac{\partial \psi}{\partial r} = B, & \omega = 0 & \text{on } \Gamma_1. \end{array} \tag{2.4}$$

2.3. *Joukowski conformal map*

The Joukowski map is defined on the exterior of the unit disk ($\mathbb{C} \setminus D_1$) by analytic formula $\phi(z) = z + z_0 + k^2/(z + z_0)$, where three real-valued parameters fully determine the airfoil shape: $k \geq 0$ controls the thickness, $\mu_x = \mathrm{Re}(z_0)$ controls the trailing-edge geometry and $\mu_y = \mathrm{Im}(z_0)$ introduces camber. Despite this low-dimensional

https://doi.org/10.1017/jfm.2026.11852 Published online by Cambridge University Press

parameterisation, Joukowski airfoils represent a wide variety of streamlined shapes. This is an analytical mapping, therefore its numerical evaluation is computationally highly efficient and precise.

Since conformality requires a non-zero derivative throughout the domain, constraints on k and z_0 must be imposed. For a conformal map from the exterior of the unit disk to the exterior of the airfoil, two conditions must hold: the shifted centre z_0 must lie inside the unit disk, ensuring that the denominator $z + z_0$ is non-vanishing in $\mathbb{C} \setminus D_1$, and $\widetilde{\phi'(z)} \neq 0$ throughout $\mathbb{C} \setminus D_1$.

Preliminary computations over the full parameter space, consistent with Sunada *et al.* (1997), confirm that an airfoil with a cusped trailing edge ($\mu_x \leq 0$) and upward camber ($\mu_y \geq 0$) achieves higher performance metrics; the parameter space is therefore restricted to

$$\mu_x \in [-1, 0], \quad \mu_y \in [0, \sqrt{1-\mu_x^2}\,), \quad k \in [0, \sqrt{1-\mu_y^2} - |\mu_x|\,). \tag{2.5}$$

The airfoil thickness decreases monotonically as k increases toward its upper bound; in the limit $k \to \sqrt{1-\mu_y^2} - |\mu_x|$ the airfoil degenerates to a flat plate.

Two further operations complete the map definition: normalisation to the unit chord and introduction of the angle of attack α. Defining $c = |z_{x_{max}} - z_{x_{min}}|$ as the distance between the leftmost and rightmost points, which coincides with the chord length for the thin airfoils considered here, the normalised map is $\widehat{\phi(z)} := \widetilde{\phi(z)}/c$. The angle of attack α is then introduced by composing $\widehat{\phi}$ with a rigid rotation: $\phi(z) := \widehat{\phi(z)}e^{i\alpha}$.

The composite normalised Joukowski map, with α as an additional parameter, thus takes the form

$$\phi(z) = \frac{e^{i\alpha}}{|z_{x_{max}} - z_{x_{min}}|}\left(z + z_0 + \frac{k^2}{z + z_0}\right), \tag{2.6}$$

with the parameter constraints given by (2.5).

2.4. *Wegmann transform*

Joukowski mapping provides control over the two most important geometric parameters: thickness and camber. However, it does not allow independent variation of the chordwise position of maximum camber p, which is known to be a third key parameter for thin airfoils. To investigate the effect of p, we generate the target profile from a four-parameter family and compute the corresponding map numerically following Wegmann (1986).

The airfoil is parametrised similarly to NACA profiles. The mean camber line $y_c(x)$, with maximum camber f at chordwise position p is defined as

$$y_c(x) = \begin{cases} \dfrac{f}{p^2}\left(2px - x^2\right), & x < p, \\ \dfrac{f}{(1-p)^2}\left(1 - 2p + 2px - x^2\right), & x \geq p, \end{cases} \tag{2.7}$$

and a symmetric thickness distribution $y_t(x)$ is added normal to it. The thickness follows the NACA four-digit polynomial, with a factor $(1-x)^{q-1}$ controlling trailing-edge closure

$$y_t(x) = \frac{t}{0.2}\,(1-x)^{q-1}\left(0.2969\sqrt{x} - 0.1260\,x - 0.3516\,x^2 + 0.2843\,x^3 - 0.1015\,x^4\right). \tag{2.8}$$

https://doi.org/10.1017/jfm.2026.11852 Published online by Cambridge University Press

The exponent q controls the trailing-edge shape: $q = 1.5$ gives a Joukowski-like cusp, $q = 1$ the wedge of the standard NACA series. We fix $t = 0.01$ and $q = 1.5$ throughout, leaving (f, p, α) as free parameters. The resulting profiles have the leading-edge radius of $\approx$0.011 % of the chord length and the maximum thickness near the leading edge of $\approx$1.2 % of the chord length. The map is then computed in two steps. First, the inverse Kármán–Trefftz map is computed

$$\frac{z-1}{z+1} = \left(\frac{w-1}{w+1}\right)^{1/n}, \quad n = 2 - \frac{\tau}{\pi}, \tag{2.9}$$

with τ defining the trailing-edge wedge angle, which the algorithm measures from the surface tangents at the trailing edge of each profile. For the cusped trailing edges considered here ($q = 1.5$), τ is small and the exponent is close to 2. This map removes the trailing-edge corner and deforms the airfoil Γ into a smooth near-circular contour $\eta(s)$ parametrised by arclength $s \in [0, 2\pi)$. Second, Wegmann's algorithm computes the exterior map g from the unit circle onto this near circle. The map must project each boundary point e^{it} to a point on the contour

$$g(\mathrm{e}^{it}) = \eta(S(t)), \tag{2.10}$$

where the boundary correspondence $S(t)$ is the unknown. Requiring g to be analytic outside the unit circle turns (2.10) into a nonlinear equation for $S(t)$, which Wegmann's method solves by iteration. The converged map is represented as a Laurent series, $g(w) = m_0 w + \sum_{k=0}^{\infty} c_k\, w^{-k}$, of which we retain the first 80 coefficients. Composing g with the forward Kármán–Trefftz transformation (2.9) results in the conformal map from the exterior of the unit circle directly onto the exterior of the airfoil, yielding $\phi(z)$ analogous to the Joukowski map of § 2.3.

2.5. *Numerical method*

The nonlinear system (2.4) is solved by Newton–Raphson iteration with backtracking line search. Because convergence is sensitive to the initial guess, different initialisation procedures are used for low and high Reynolds numbers. For $Re < 200$, the potential-flow solution is used as the initial guess. For higher Re, a continuation strategy is employed over an increasing sequence of Reynolds numbers, $Re_1 < Re_2 < \cdots < Re_{target}$, with each converged solution used for the next step. As an example, to reach $Re = 1000$, the sequence $200 \to 300 \to 500 \to 750 \to 1000$ is used.

The linearised system is discretised with second-order finite differences on a uniform $N_r \times N_s = 450 \times 600$ grid with a periodic boundary condition in the circumferential direction. The outer boundary is placed at the distance of $114c$ and $78c$ away from the airfoil for $Re < 150$ and $Re \geq 150$, respectively, where the larger domain compensates for the slower decay of velocity perturbations in the low-Re regime (Khalili & Liu 2017). The conformal stretching concentrates nodes near the wall: the first off-wall layer thickness ranges from $1.3 \times 10^{-4}c$ near the trailing-edge cusp to $7.0 \times 10^{-3}c$ along the remainder of the chord. Solver accuracy is confirmed in Appendix.

Once the vorticity–streamfunction system is solved, the lift and drag coefficients are recovered from the surface pressure P and wall shear stress τ_w. We use the non-dimensionalisation $\rho_\infty = 1$, $U_\infty = 1$, $c = 1$, under which the dynamic pressure is $q_\infty = 1/2$, dynamic viscosity is $\mu = 1/Re$ and the lift and drag coefficients reduce to $C_L = 2F_L$, $C_D = 2F_D$, where F_L and F_D are lift and drag forces.

The surface pressure satisfies $\mathrm{d}P/\mathrm{d}s = -(1/Re)(\partial\omega/\partial r)|_\Gamma$, which is obtained from the tangential momentum equation at the wall, with gauge condition $\int_\Gamma P\, \mathrm{d}s = 0$. The wall

https://doi.org/10.1017/jfm.2026.11852 Published online by Cambridge University Press

shear stress is $\tau_w = \omega\sqrt{\det \boldsymbol{J}}/Re$. The lift and drag coefficients follow from integrating the pressure and shear-stress contributions over the airfoil surface, with the Jacobian components A and B entering through the coordinate transformation

$$C_D = -2\int_\Gamma PA\,\mathrm{d}s - \frac{2}{Re}\int_\Gamma \omega B\,\mathrm{d}s, \quad C_L = -2\int_\Gamma PB\,\mathrm{d}s + \frac{2}{Re}\int_\Gamma \omega A\,\mathrm{d}s. \tag{2.11}$$

3. Optimisation

We optimise airfoil profiles over $Re \in [1, 3000]$ in two independent sets of numerical experiments to maximise two different performance metrics: C_L/C_D (in the literature termed as lift-to-drag ratio, or glide ratio) and $C_L^{3/2}/C_D$ (termed as endurance factor, or power factor). These are the two most commonly used objectives when designing airfoils for regimes that typically constitute most of the flight duration, e.g. cruise and loitering flight. Since direct search over the full four-parameter space $(k, \mu_x, \mu_y, \alpha)$, as defined in (2.6), is computationally expensive, we progressively narrow the parameter domain as follows.

We begin by analysing symmetric airfoils: $\mu_y = 0$, $\mu_x = 0$. This reduction to a two-parameter problem (k, α) makes it feasible to construct the objective function over a structured grid and examine its global behaviour. The computed objective surfaces reveal that, within the class of symmetric airfoils, the highest performance is consistently achieved for zero-thickness airfoils, corresponding to a flat plate. To determine whether this tendency persists when camber and trailing-edge geometry are free, we proceed to the full four-parameter space of Joukowski foils, employing three complementary global search strategies in parallel: Sobol sequence sampling, covariance matrix adaptation evolution strategy and Bayesian optimisation. All three strategies consistently identify zero-thickness airfoils with $\mu_x \approx 0$ as optimal across the entire Re range, in agreement with existing results for low-Reynolds-number airfoils (Sunada *et al.* 1997). Accordingly, the parameter μ_x is set to 0 and k is set to the zero-thickness limit for each μ_y, as given by the upper bound in (2.5). This reduction implies $k = \sqrt{1-\mu_y^2}$ (in practice, k is set to $\sqrt{1-\mu_y^2} - \varepsilon$ with $\varepsilon = 10^{-7}$ to avoid the map singularity at the boundary of the admissible domain; this has no measurable effect on the aerodynamic coefficients), leaving μ_y as the only geometric parameter of the airfoil. For a thin Joukowski profile, μ_y is related to the camber f through the image of the top of the circle ($z = \mathrm{i}$)

$$f = \mathrm{Im}\big(\mathrm{i} + \mu_y\mathrm{i} + \big(1-\mu_y^2\big)/(\mathrm{i}+\mu_y\mathrm{i})\big)/c = \mu_y/(2k), \tag{3.1}$$

which inverts to give $\mu_y = 2f/\sqrt{1+4f^2}$. The optimisation thus reduces to a two-parameter problem in (f, α) space. A structured high-resolution grid search is performed over this plane with steps $\Delta\alpha = 0.5°$ and $\Delta f = 0.5\,\%$, within windows centred on the regions identified by the global search.

4. Results and discussion

Let us denote as $\alpha_{opt,G}$ and $f_{opt,G}$, respectively, the angle of attack and camber that maximise C_L/C_D. Similarly, $\alpha_{opt,E}$ and $f_{opt,E}$ will stand for the values that maximise $C_L^{3/2}/C_D$. We will also use shorter notations α_{opt} and f_{opt} in statements that apply to both maximisation objectives. The results of the high-resolution grid search optimisation are presented in figure 2. Solid lines correspond to the Joukowski airfoils. Point markers

https://doi.org/10.1017/jfm.2026.11852 Published online by Cambridge University Press

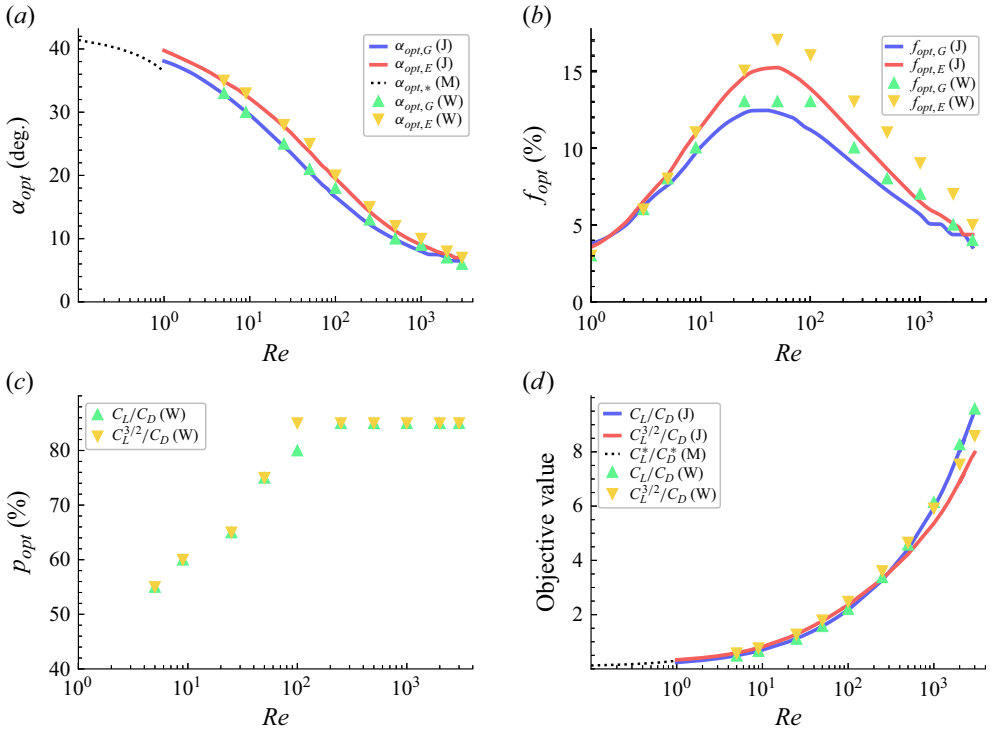


Figure 2. Results of optimisation of C_L/C_D (subscript G) and $C_L^{3/2}/C_D$ (subscript E). (a) Optimal angle of attack α_{opt} as a function of Re; (b) optimal camber f_{opt} as a function of Re; (c) optimal chordwise position p_{opt} of the maximum camber as a function of Re; (d) maximum C_L/C_D and $C_L^{3/2}/C_D$ as functions of Re. Solid blue and red lines and the letter J correspond to the results obtained for Joukowski airfoils. Green and yellow triangular markers and the letter W correspond to the results of calculations using the Wegmann method with the chordwise position p of the maximum camber treated as one of the optimisation parameters. Black dotted lines and letter M represent the asymptotic formula for the maximum C_L^*/C_D^* value and corresponding $\alpha_{opt,*}$ for a flat plate. The position of the maximum camber of thin Joukowski foils is constrained at $p = 50\,\%$ and therefore not shown on the plot.

correspond to the extended optimal shapes obtained with the position of the maximum camber p as an additional optimisation parameter, by employing a Wegmann transform. For both airfoil families and both objective functions, the results are qualitatively the same and quantitatively close. Let us first discuss the results obtained for Joukowski airfoils. As Re increases from 1 to 3000, α_{opt} decreases monotonically from 39° to 6°, with a maximum difference between $\alpha_{opt,E}$ and $\alpha_{opt,G}$ of 3.2° at $Re = 50$. The parameter f_{opt} follows a bell-shape curve, with $f_{opt,G}$ and $f_{opt,E}$ behaving nearly identically at the boundaries of the Re range considered: starting and ending at 3.5 % at $Re = 1$ and $Re = 3000$. Significant differences appear only near the peaks: $f_{opt,G} = 12.3\,\%$ at $Re = 40$ and $f_{opt,E} = 15.2\,\%$ at $Re = 50$, and a maximum difference of 2.9 % at $Re = 50$.

When the position p of the maximum camber is treated as an adjustable parameter, for the flow regimes near $Re = 10$, the optimal position of the maximum camber is near 50 % chordwise. However, for larger Re, optimal position of the maximum camber progressively shifts downstream toward the trailing edge. The cambers f are larger but the angles of attack α are the same as for the Joukowski airfoils. The objective function values are slightly greater than for the Joukowski airfoils. The latter results, however, have been obtained with the fixed maximum thickness near the leading edge of 1.2 % of the chord

https://doi.org/10.1017/jfm.2026.11852 Published online by Cambridge University Press

length as required for the numerical mapping, and this value is considerably larger than the Joukowski airfoil thickness. It can be postulated that trends shown in figure 2 might be generally representative of optimal thin airfoils.

In the low-Reynolds-number regime, the Oseen approximation is valid, and the numerical results show that $f_{opt} \to 0$, meaning the optimal shape reduces to a flat plate. It is therefore natural to compare the numerical results against the analytical solution derived by Miyagi (1964) for the lift and drag of a flat plate under the Oseen approximation: $C_D^* = (16\pi/Re)((2S_1 - 1 - \cos 2\alpha)/(4S_1^2 - 2(1 + \cos 2\alpha)))$, $C_L^* = (16\pi/Re)((\sin 2\alpha)/(4S_1^2 - 2(1 + \cos 2\alpha)))$, where $S_1 = \ln(16/Re) - \gamma$, with γ denoting the Euler–Mascheroni constant. Maximising C_L^*/C_D^* with respect to α yields the optimal angle, $\alpha_{opt,*} = \arctan\sqrt{1 - 1/S_1}$, which satisfies $\alpha_{opt,*} \to 45°$ as $Re \to 0$, explaining the large optimal angles of attack observed at the lower end of the Reynolds-number range. Since S_1 is a decreasing function of Re, $\alpha_{opt,*}$ itself decreases monotonically with Re, consistent with the numerical results.

The non-monotonic behaviour of f_{opt} arises from a competition between positive and negative aerodynamic effects. The benefits of non-zero camber are twofold. First, curvature enhances the inertial pressure differential between lower and upper surfaces. Second, these enhanced pressure forces near the leading edge are oriented vertically, contributing to C_L to a greater extent. On the downside, greater pressure differential on a cambered foil entails larger adverse pressure gradient in the aft portion of it, which leads to flow separation and increased drag. As Re increases from the lower end, increased inertia boosts the curvature-induced excess C_L. At the same time, viscous diffusion remains strong enough to mitigate flow separation even at large f and α, permitting highly cambered airfoils to remain near optimal. Together, these effects drive f_{opt} upward until $Re \approx 40{-}50$.

Beyond this peak, the trend reverses: as inertia becomes dominant, viscosity can no longer resist and the flow separates at large f and α without reattachment. Both f_{opt} and α_{opt} decline toward lower values. Flow detachment simultaneously reduces lift and increases drag, impairs both C_L/C_D and $C_L^{3/2}/C_D$; any (f, α) combination at which the bubble opens is suboptimal. The optimal airfoils, therefore, reside in the attached-flow regime, which justifies the use of the steady solver in this study. At $Re = 100$, the optimal cambered airfoil ($f_{opt,G} = 11.2\,\%$, $\alpha = 16.6°$) already carries a trailing-edge recirculation bubble, visible in the streamlines (figure 3*b*,*c*), yet the flow remains steady. This airfoil achieves 17 % higher C_L/C_D than the flat plate (figure 3*a*,*d*), confirming that moderate camber remains beneficialeven as a separation bubble begins to form. For the optimal shape found at $Re = 3000$ ($f_{opt,G} = 3.5\,\%$, $\alpha = 6°$), this was confirmed by supplementary unsteady numerical simulations using OpenFOAM (see https://osf.io/y4pr8), in which the fluctuation amplitude did not exceed 0.2 % of the respective mean values. The Reynolds number based on the perpendicular projection of the chord, $Re_\perp = Re \sin\alpha$, equals 314 in the optimal case at $Re = 3000$, and decreases with the decreasing Re, further supporting the steady flow assumption.

At low Re, strong viscous diffusion spreads the C_L/C_D and $C_L^{3/2}/C_D$ maxima broadly across the (f, α) space; as inertia strengthens with Re, the maxima sharpen, making a geometrically precise optimal airfoil identifiable. This is illustrated in figure 4, which shows contour plots of C_L/C_D at $Re = 10$, 100 and 500. All panels span equal ranges $\delta f \times \delta\alpha = 7\,\% \times 10°$, centred on (f_{opt}, α_{opt}) at each Re, enabling direct comparison of landscape sharpness. At $Re = 10$, C_L/C_D varies by less than 5 % across the displayed range, meaning that a wide number of (f, α) combinations yields nearly identical performance. As Re increases, the maximum becomes more distinct: at $Re = 100$ the

https://doi.org/10.1017/jfm.2026.11852 Published online by Cambridge University Press

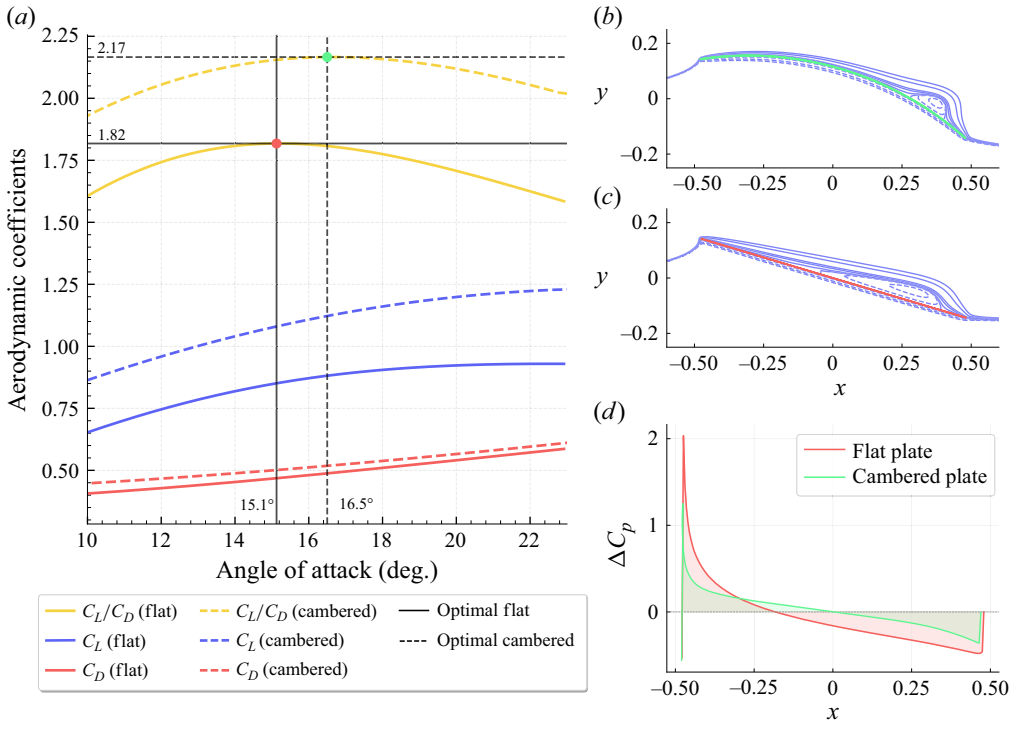


Figure 3. (*a*) Lift, drag and lift-to-drag ratio curves as functions of α at $Re = 100$ for the flat and optimal cambered profiles, with optimal α and values of C_L/C_D marked. (*b*,*c*) Streamlines for the optimal cambered and flat profiles respectively, shown at levels 0, $\pm 10^{-5}$, $\pm 5 \times 10^{-5}$, $\pm 10^{-4}$, $\pm 5 \times 10^{-4}$, $\pm 10^{-3}$. (*d*) Pressure coefficient difference along the chord for both profiles.

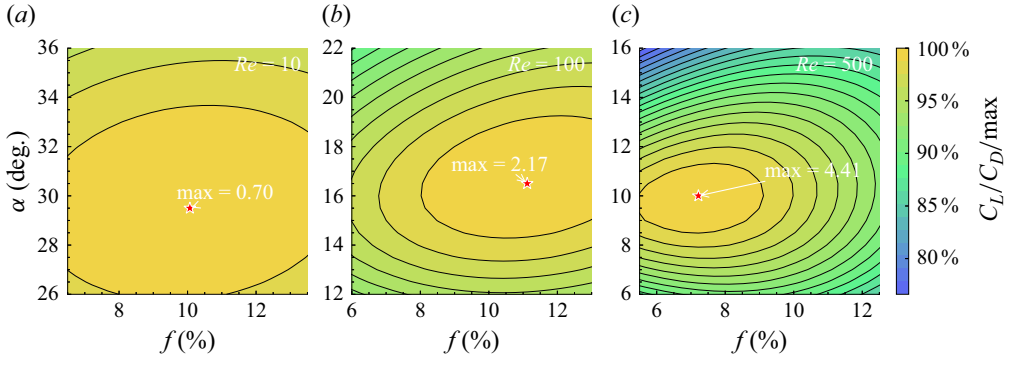


Figure 4. Counterplots of C_L/C_D normalised by its maximum value, in the (f, α) parameter space: (*a*) for $Re = 10$; (*b*) for $Re = 100$; (*c*) for $Re = 500$. Stars mark the (f^*, α^*) in each case. All panels span equal areas of the (f, α) parameter space.

variation reaches 10 %, and at $Re = 500$ it is 25 %. This progressive sharpening has a direct implication: below $Re \approx 100$, performance is insensitive to the precise choice of f and α, whereas above $Re \approx 500$, the sharp peak singles out a physically distinguished (f, α) combination, making optimisation both meaningful and effective.

https://doi.org/10.1017/jfm.2026.11852 Published online by Cambridge University Press

5. Conclusion

Optimisation of Joukowski airfoils across $Re \in [1, 3000]$ within the steady, laminar, incompressible Navier–Stokes model has revealed features and trends of optimal airfoils that are common to both the C_L/C_D and $C_L^{3/2}/C_D$ maximisation in the intermediate-Reynolds-number range. Zero-thickness cambered airfoils are optimal for both C_L/C_D and $C_L^{3/2}/C_D$ throughout the entire intermediate-Re range. This result is confirmed by three independent global search strategies. The optimal angle of attack decreases monotonically with Re, while the optimal camber follows a bell-shaped curve. At $Re \lesssim 10$, near-flat plates ($f \lesssim 11\,\%$) at high angle of attack ($\alpha \approx 35{-}39°$) are optimal. As Re increases, optimal camber attains a peak of 12.3 % (C_L/C_D) and 15.2 % ($C_L^{3/2}/C_D$) at $Re \approx 40{-}50$, marking the transition from viscosity-dominated to inertia-dominated flow. At $Re = 3000$, both f and α converge toward the slightly cambered ($\sim$4 %) low-α ($\sim 6°$) geometry, in close agreement with the optimal airfoils identified by Sunada *et al.* (1997) at $Re = 4000$ and consistent with the slightly cambered geometry characteristic of conventional low-speed airfoils. Another useful property is the sharpness of the C_L/C_D and $C_L^{3/2}/C_D$ maxima in (f, α) space. Below $Re \approx 100$, geometric precision is aerodynamically unimportant: performance varies by less than 10 % across a broad neighbourhood of the optimum. Above $Re \approx 500$, the objective functions have a distinct optimum, with a 25 % change in performance across a neighbourhood of the same size. The optimisation then reveals a distinct optimal shape, clearly superior to neighbouring designs in terms of aerodynamic performance. After extending the parameter space by including the chordwise position p of the maximum camber as an adjustable parameter, the trends of optimal α and f have remained the same, although the values of f_{opt} have increased by a few per cent. In addition, these optimisation runs have revealed a trend for the optimal chordwise position of the maximum camber to shift, with increasing Re, towards the trailing edge, which has not been reported in earlier studies.

Declaration of interests. The authors report no conflict of interest.

Data availability statement. The solver source code is accessible on GitHub. Datasets and other supplementary information can be downloaded from https://osf.io/y4pr8.

AI statement. AI tools have been used in the writing process.

Appendix. Solver verification

The solver is implemented in Python and is validated against three benchmark cases: flow past a circular cylinder, flow past a thin flat plate and flow past a NACA 0012 airfoil. Figure 5(*a*) shows drag coefficients for the cylinder at $Re = 7$–40 in close agreement with the solutions of Dennis & Chang (1970), Nieuwstadt & Keller (1973) and Dennis (1976). Figure 5(*b*,*e*) compares lift and drag coefficients for the flat plate at $Re = 5$, 10, 20 with results of In *et al.* (1995), showing good agreement across all α. Figure 5(*c*,*f*) compares lift and drag coefficients for the NACA 0012 airfoil at $Re = 10$, 100, 250, 500 with results of Srinath & Mittal (2009). The coefficients agree closely at $Re = 100$, 250, 500 for all α; at $Re = 10$ the agreement is weaker, which we attribute to the comparatively small computational domain (10 chord lengths) used by Srinath & Mittal (2009), insufficient to fully capture the far-field decay of the flow at this low Reynolds number. Mesh convergence is demonstrated in figure 5(*d*) for the cylinder at $Re = 40$, confirming second-order spatial accuracy.

https://doi.org/10.1017/jfm.2026.11852 Published online by Cambridge University Press

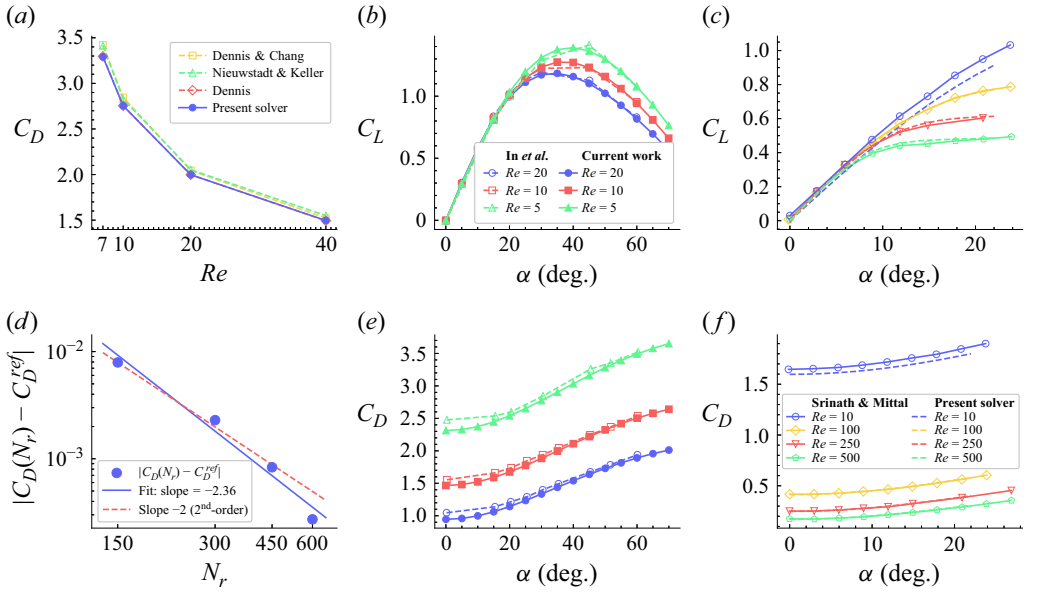


Figure 5. Solver validation. (*a*) Drag coefficient for flow past a circular cylinder at $Re = 7$, 10, 20, 40, compared with Dennis & Chang (1970), Nieuwstadt & Keller (1973) and Dennis (1976). (*b*,*e*) Lift and drag coefficients versus angle of attack α for a thin flat plate at $Re = 5$, 10, 20, compared with In *et al.* (1995). (*c*,*f*) Lift and drag coefficients versus α for NACA0012 at $Re = 10$, 100, 250, 500, compared with Srinath & Mittal (2009). (*d*) Mesh convergence at $Re = 40$, showing second-order behaviour.

References

Dennis, S.C.R. 1976 A numerical method for calculating steady flow past a cylinder. In *Proceedings of the Fifth International Conference on Numerical Methods in Fluid Dynamics*, (ed. A.I. Van De Vooren & P.J. Zandbergen), Lecture Notes in Physics, vol. 59, pp. 165–172. Springer.

Dennis, S.C.R. & Chang, G.Z. 1970 Numerical solutions for steady flow past a circular cylinder at Reynolds numbers up to 100. *J. Fluid Mech.* **42**, 471–489.

In, K.M., Choi, D.H. & Kim, M.-U. 1995 Two-dimensional viscous flow past a flat plate. *Fluid Dyn. Res.* **15** (1), 13–24.

Khalili, A. & Liu, B. 2017 Stokes' paradox: creeping flow past a two-dimensional cylinder in an infinite domain. *J. Fluid Mech.* **817**, 374–387.

Miyagi, T. 1964 Oseen flow past a flat plate inclined to the uniform stream. *J. Phys. Soc. Japan* **19** (6), 1063–1073.

Nieuwstadt, F. & Keller, H.B. 1973 Viscous flow past circular cylinders. *Comput. Fluids* **1** (1), 59–71.

Srinath, D.N. & Mittal, S. 2009 Optimal airfoil shapes for low Reynolds number flows. *Intl J. Numer. Meth. Fluids* **61** (4), 355–381.

Sunada, S., Sakaguchi, A. & Kawachi, K. 1997 Airfoil section characteristics at a low Reynolds number. *J. Fluids Engng* **119** (1), 129–135.

Wegmann, R. 1986 An iterative method for conformal mapping. *J. Comput. Appl. Maths* **14** (1–2), 7–18.

https://doi.org/10.1017/jfm.2026.11852 Published online by Cambridge University Press